

# Development of Super-resolution Ultrasound Imaging based on Synthetic Aperture System via Experiments and Simulations

Jing Zhu<sup>a</sup>, Norio Tagawa

Graduate School of System Design, Tokyo Metropolitan University,  
6-6 Asahigaoka, Hino, Tokyo, 191-0065, Japan

<sup>a</sup>E-mail: zhu-jing@ed.tmu.ac.jp

**Abstract**—Synthetic aperture (SA) imaging is a conventional technique that is used in ultrasound imaging to overcome low frame rate problems by applying various modifications. Another approach to provide improved image spatial resolution, called the super-resolution frequency modulation (FM)-chirp correlation method (SCM), which is based on the multiple signal classification (MUSIC) algorithm, has also been proposed. We have previously proposed a scheme called the SA-SCM to extend the SCM to the SA system and improve its range resolution with high frame rates. However, the SA-SCM was found to have discontinuities in the lateral direction because the SCM was performed line by line along the range direction. In this work, another combination of the SA and SCM techniques is studied. The performances of the SCM-SA and SCM-weighted SA methods are discussed based on the results of experiments and finite element method (FEM) simulations. The results show that the proposed methods avoid a large number of SA processing steps and provide a super range resolution performance with no discontinuities in the lateral direction.

**Index Terms**—Synthetic aperture imaging, super-resolution, MUSIC algorithm.

## I. INTRODUCTION

Ultrasound imaging is an effective and intuitive imaging method and is widely used in medical diagnosis [1] and nondestructive testing (NDT) applications [2]. Therefore, it is important to continue to improve the quality of ultrasound imaging parameters such as the frame rate and the spatial resolution. While the quality of ultrasound imaging has been enhanced over the past few decades [3] [4], there is still considerable potential for further improvement. Therefore, the goal of this work is to realize super range resolution imaging for strong reflection imaging of targets such as organ boundaries and blood vessel walls. In this study, a compound method that combines synthetic aperture (SA) imaging with the super-resolution frequency modulation (FM)-chirp correlation method (SCM) is proposed.

The SA imaging method has been used in ultrasound imaging since the 1980s [5]. Since then, an increasing number of studies have been completed on the SA method for medical imaging [6]. In SA systems, a high

signal-to-noise (SNR) image can be reconstructed from multiple low-SNR images that were acquired using multiple sub-apertures [7]. Recent developments in these studies have brought benefits in terms of enhanced lateral resolution [8], SNR [9] and depth penetration [10].

We have also studied the SCM [11], which is based on the multiple signal classification (MUSIC) algorithm that was introduced by Schmidt [12] and was initially used for electromagnetic waves. At present, this algorithm plays an important role in sound wave applications [13]. The most important feature of the SCM is that multiple transmissions and receptions (TRs) with different carrier frequencies are performed to distinguish the waves reflected from the scatterers at the different positions in the echo with a resolution that corresponds to the wavelength of the carrier wave. Specifically, focused pulses are transmitted to aid with resolution improvement in the SCM. Therefore, the SCM requires multiple TRs for each imaging line. To reduce the number of TRs that are required for the SCM, we previously proposed a scheme for extension of the SCM to the SA system called the SA-SCM [14]. In this scheme, divergent waves are transmitted and it has been demonstrated using simulations that the SA-SCM offers both a high frame rate and super-resolution performance along the range direction [15]. However, the SA-SCM method has faced challenges raised by discontinuities that occur in the lateral direction because the SCM processing is performed line by line along the range direction.

To avoid these lateral discontinuities and reduce the number of SA processing steps, we can reverse the processing order of the SCM and the SA in the SA-SCM method; the resulting method is called the SCM-SA method in this study. In this case, the SCM is applied first to each echo that is measured at each transducer element, and the results from the SCM are then used as the input for SA processing. However, the SCM results at each element contain no phase information and are simply positively-valued signals. Therefore, the cancellation of the positive and negative signals, which is expected to reduce the number of unwanted signals, is less likely to occur in the SCM-SA method. For further improvements, a strategy in which the SCM results are used as weights for SA processing can be considered, and this version is called the SCM-weighted SA method. The

SCM-SA and SCM-weighted SA methods proposed here are expected to provide better resolution performances than conventional SA imaging. Additionally, because SCM processing is performed first for each element, the number of SA operations can be reduced. Therefore, these methods also offer the potential to reduce the computation time required for each image. In this study, we explain the proposed methods, confirm the performances of these methods using experimental systems and finite element method (FEM) simulations and summarize the conclusions drawn from our findings.

## II. METHODS

### A. Outline of SA Imaging

SA imaging is based on use of the delay-and-sum (DAS) beamforming algorithm [16] to form the final image. The DAS is a signal processing technique that is used to generate images from the echoes that are received by all the transducer elements individually. The delay times of the echoes that are received from the same target by each transducer element are different, which means that when these echoes are summed together, one particular portion of the target is amplified while the other parts are weakened. In this study, unfocused beam transmission and DAS beamforming techniques are applied to SA imaging.

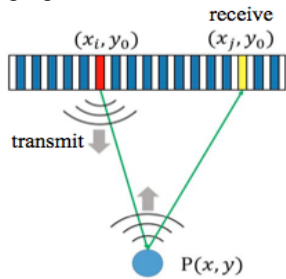


Fig. 1. Illustration of synthetic aperture.

As shown in Fig. 1, a spherical wave is emitted by a single element in the linear array and propagates to the target, which is located far away from the probe. After a complex combination of reflection, refraction, scattering and attenuation, the echo from the target is received by all elements in the linear array. Suppose that the receiving focal point is located at the position  $(x, y)$  in front of the array; the amount of delay time that must be applied to each array element relative to the focal point can be calculated using [17]:

$$t = \frac{\sqrt{(x_i - x)^2 + (y_0 - y)^2} + \sqrt{(x_j - x)^2 + (y_0 - y)^2}}{c} \quad (1)$$

where  $(x_i, y_0)$  represents the coordinates of the  $i$ th element for transmission,  $(x_j, y_0)$  represents the coordinates of the  $j$ th element for reception, and  $c$  is the speed of sound in the medium.

### B. Outline of SCM

We now introduce the actual implementation of the SCM used in ultrasound imaging. The SCM can achieve

super-resolution imaging using the phase information obtained from the carrier waves after the FM-chirp echo signals are compressed.

First, assuming that the FM-chirp signal is transmitted at a centre frequency of  $\omega_0$ :

$$s(t) = \text{Re}[x(t)e^{j\omega_0 t}] \quad (2)$$

and then the echo signal  $y(t)$  obtained in the radio-frequency (RF)-band from  $D$  scatterers can be described as follows:

$$y(t) = \int_{-\infty}^{\infty} h(t)s(t-t)dt, \quad h(t) = \sum_{i=1}^D h_i \delta(t-t_i) \quad (3)$$

where  $h(t)$  is an impulse response that indicates the reflections from the scatterers,  $\{t_i\}$  is a set of propagation delays that must be estimated, and  $\delta(\cdot)$  represents the Dirac delta function.

The received echo that is calculated from the in-phase (I) and quadrature-phase (Q) components in the baseband is denoted by  $v(t)$ , while the compressed  $v(t)$  signal is denoted by  $z(t)$ .

$$n(t) = \sum_{i=1}^D h_i e^{-j\omega_0 t_i} x(t-t_i) + n(t) \quad (4)$$

$$z(t) = \sum_{i=1}^D h_i e^{-j\omega_0 t_i} r(t-t_i) + m(t) \quad (5)$$

Here,  $z(t)$  denotes the complex-valued delay profile, while  $r(t)$  represents the complex-valued auto-correlation function of the baseband modulation signal  $x(t)$ . It is supposed here that the noise  $n(t)$  has a zero mean and a variance of  $\sigma^2$ , that it is uncorrelated with the signals and uncorrelated with each other. Therefore,  $m(t)$  is the complex-valued cross-correlation of  $x(t)$  with  $n(t)$ .

Because the compressed echo signal can be expressed as shown in equation (5), it can then be written using the following vector representation:

$$\mathbf{z} = \mathbf{G}\mathbf{g} + \mathbf{m} \quad (6)$$

where  $\mathbf{z} = [z(t_1), z(t_2), \dots, z(t_M)]^T$  is a compressed echo vector. In terms of the array manifold matrix,  $\mathbf{\Gamma} = [\mathbf{r}_1, \mathbf{r}_2, \dots, \mathbf{r}_D]$  and  $\mathbf{g} = [h_1 e^{-j\omega_0 t_1}, h_2 e^{-j\omega_0 t_2}, \dots, h_D e^{-j\omega_0 t_D}]^T$  are used.  $\mathbf{r}_i = [r(t_1-t_i), r(t_2-t_i), \dots, r(t_M-t_i)]^T$  is a steering vector, while  $\mathbf{m} = [m(t_1), m(t_2), \dots, m(t_M)]^T$  is a noise vector. Here,  $M$  and the superscripted T denote the number of sampled points and the matrix transpose, respectively.

In this case, the spatial covariance matrix can be analysed using the following equation:

$$\mathbf{R} = E[\mathbf{z}\mathbf{z}^H] = \mathbf{G}\mathbf{G}^H + \mathbf{R}_n \quad (7)$$

where  $\mathbf{G} = E\{\mathbf{g}\mathbf{g}^H\}$ ,  $\mathbf{R}_n = E\{\mathbf{m}\mathbf{m}^H\} = \sigma^2 \mathbf{R}_0$ , the superscripted H denotes the Hermitian operator, and

$E[\cdot]$  denotes the expectation operator.  $\sigma^2$  and  $\mathbf{R}_0$  are the variance of the noise and a symmetrical matrix consisting of  $r(t)$ , respectively.

Then, from the general eigenvalue equation:

$$\mathbf{R}\mathbf{e}_i = \lambda_i \mathbf{R}_0 \mathbf{e}_i; i = 1, 2, \dots, M \quad (8)$$

the eigenvalues  $\{\lambda_i\}$  ( $i=1,2,\dots, M$ ) and the corresponding eigenvectors  $\{\mathbf{e}_i\}$  ( $i=1,2,\dots, M$ ) can be calculated. The  $M$  eigenvalues are then sorted into descending order, where  $\mathbf{R}$  contains  $D$  eigenvalues that are much larger than  $\sigma^2$  and the eigenvectors correspond to the signal subspace. The remaining  $M-D$  eigenvalues are approximately equal to  $\sigma^2$  and the corresponding eigenvectors span to the noise subspace.

After eigen-decomposition, the orthogonality between the steering vector and the noise subspace can be used. Finally, a super-resolution delay profile denoted by  $S(t_i)$  can be defined using the MUSIC algorithm as:

$$S(t_i) = \frac{\mathbf{r}_i^H \mathbf{R}_0^{-1} \mathbf{r}_i}{\sum_{j=D+1}^M |\mathbf{r}_i^H \mathbf{e}_j|^2} \quad (9)$$

In general applications,  $D$  should correspond to the number of target signals contained in the echo and should thus be determined using, for example, Akaike's information criterion (AIC) [18] or the minimum description length (MDL) criterion [19].

To estimate  $\mathbf{R}$  while avoiding the problem where the rank of  $\Gamma\Gamma^H$  is deficient, which may affect the path coherence, we use a frequency smoothing method that is described in the next section. The smoothed covariance matrix denoted by  $\mathbf{R}^*$  can then be calculated using:

$$\mathbf{R}^* = \frac{1}{N} \sum_{j=1}^N \mathbf{z}_j \mathbf{z}_j^H \quad (10)$$

where  $\mathbf{z}_j$  is the echo vector of the  $j$ -th transmission with its carrier frequency, and  $N$  is the number of transmissions. Therefore, an ensemble average of  $\mathbf{R}^*$  can be used to estimate  $\mathbf{R}$ .

### C. Frequency Smoothing Method

In SCM processing, the signal subspace basically must be orthogonal to the noise subspace, which means that coherent or fully correlated signals will have undesirable effects on the results. The most important aim of this study is to improve the range resolution using frequency smoothing method [11]. It should also be noted that multiple phase-shift TRs cannot be used in place of frequency changes. If multiple transmissions were to be performed with different phases rather than with different frequencies, the same phase rotation would occur simultaneously for all echoes from each scatterer; these echoes would only differ by complex number multiples and thus could be regarded as one reflected wave.

In general, SCM processing performance is better when using linear frequency smoothing or random

frequency smoothing. In this study, to emphasise avoidance of the artefacts caused by periodic frequency changes, the random frequency smoothing method shown in Fig. 2 was used.

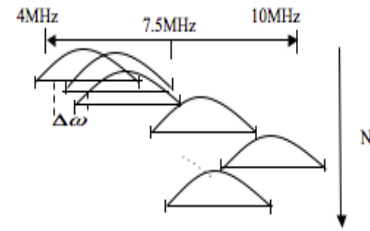


Fig. 2. Frequency smoothing method.

### D. SCM-SA and SCM-weighted SA

To reduce the number of multiple TRs required in the SCM, the SA-SCM has been successfully proposed and presented [15]. In the SA-SCM, diverging waves are transmitted; subsequently, beam reception is performed, and finally the SCM generates a super-resolution profile for each line in the imaging region. Here, the SCM processing can be regarded as a supplementary algorithm, which means that we can exchange the order in which the SA and the SCM are executed to obtain a different method, which is called the SCM-SA method. In the SCM-SA method, the SCM is applied to each echo that is received by each element; then, the resulting positive SCM profiles are used for the next SA processing stage. When the cancellation of the positive and negative signals is considered, we can use the SCM results from each element's echo as a weight for the SA processing; this is called the SCM-weighted SA method.

It should be noted that in the SCM-SA and SCM-weighted SA methods, in contrast to the SA-SCM, the transmission position at the transducer must be fixed. When different frequency pulses are transmitted from different positions, the positions of the corresponding reflected waves are shifted between the echoes of the different frequencies received by each element, and SCM processing then cannot be executed in the SCM-SA and SCM-weighted SA methods.

The proposed SCM-SA and SCM-weighted SA methods are expected to be superior to the conventional SA method from a range resolution viewpoint. In the SA-SCM, an SA is required for each of the image lines, whereas in the SCM-SA and SCM-weighted SA methods, only one SA is required per image. This means that the SCM-SA and SCM-weighted SA methods may offer further potential for reduction of the computational requirements. Furthermore, because processing is performed for each element, the discontinuities that may occur in the lateral direction in the SA-SCM can be avoided.

## III. EXPERIMENTAL

### A. Experimental Conditions

Figure 3 shows a schematic illustration of the experimental system that was used in this study. A diagnostic ultrasonic platform (RSYS0003, Microsonic

Co. Ltd., Japan) that was equipped with a linear array probe with a centre frequency of 7.5 MHz and a specific bandwidth of more than 70% (T0-1599, Nihon Dempa Kogyo Co. Ltd., Japan) was used to perform the experimental measurements.

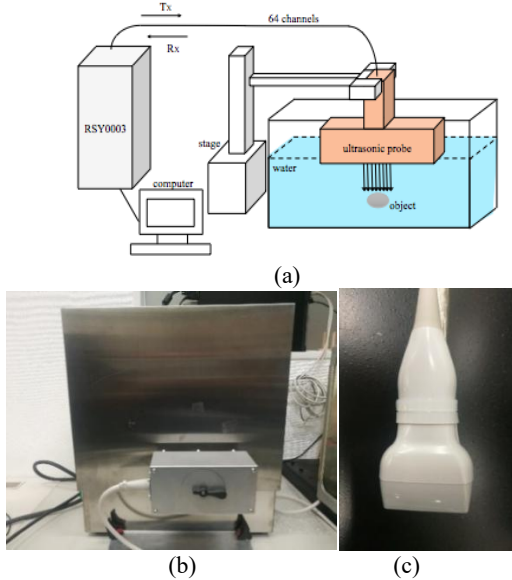


Fig. 3. Experimental conditions: (a) Experimental system used for the measurements; (b) ultrasound experimental platform RSY0003; and (c) illustration of the probe.

During the reception process, the transducer array elements were connected to 64 channels, while the beamforming and image construction procedures were performed offline using MATLAB software. The element pitch of the transducer array was 0.315 mm, which meant that the aperture width was approximately 20 mm. In addition, the sampling frequency that was used in the reception process was set at 31.25 MHz via the hardware configuration.

### B. Experimental Setup

The experimental setup used is shown in Fig. 4. FM chirp pulses that had been apodised using a Hanning window with a bandwidth of 2 MHz and a duration of 5  $\mu$ s were transmitted directly as diverging waves using a sub-aperture that was formed of eight elements and was located at the centre of the probe, while an echo was received by all 64 elements. In this study, we repeated the transmission and reception processes 15 times while randomly varying the frequency from 4 MHz to 10 MHz. Because of equipment restrictions, the experimental system was limited to  $\pm 3$  voltage levels while it also included a 0 level (giving a total of seven voltage levels) for transmission. Figure 5 shows an example of a transmitted signal. A metal rod with a vinyl coating layer and a diameter of 1.5 mm was located 15 mm away from the probe in the water and acted as the imaging target.

### C. Experimental Results

In the experiments, the eigenvalues that correspond to the signal subspace that was calculated via SCM processing in our methods are sufficiently larger than the corresponding values in the noise subspace when  $D=1$ ,

and we thus set  $D=1$  uniformly for all SCM processing. Therefore, we did not discuss the effects of use of the AIC or the MDL to determine  $D$ . In future work, however, such discussions may offer the potential to further enhance the estimation process.

Figure 6 shows an example of a compressed echo that was received by the centre element of the probe. Figure 7(a)–(d) illustrate the B-mode images that are generated using the conventional SA, the SA-SCM, the SCM-SA and the SCM-weighted SA methods proposed in this study, respectively. For the SA, the SCM-SA and the SCM-weighted SA methods, each image corresponding to each frequency was calculated, and the final B-mode images were then generated as the averages of 15 images.

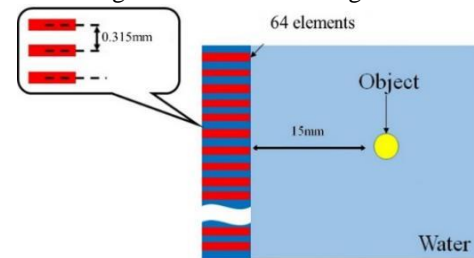


Fig. 4. Experimental setup.

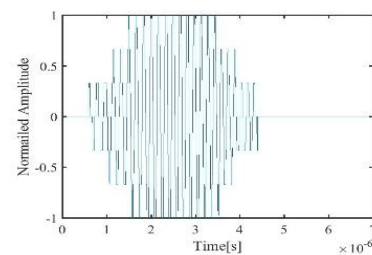


Fig. 5. Example of transmitted signal used for experiments.

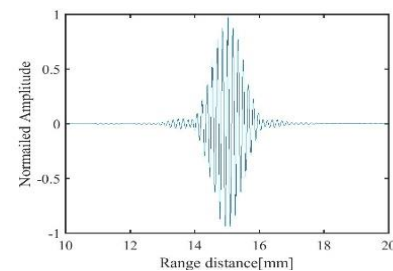


Fig. 6. Example of compressed RF echo from the wire target that was received by the centre element of the probe.

Some artefacts can be seen in these images, and these artefacts can be generated for several reasons. The fact that the element pitch is more than half of the ultrasonic wavelength and generates grating lobes could be considered to be a major cause of the artefacts observed in the results. For the SA, we used the average result from 15 images to reduce the grating lobes. As Fig. 7 shows, when the frequency increases, the element pitch is much greater than half of the ultrasonic wavelength, and thus the SA image creates increasing numbers of artefacts. For the SA-SCM, the effect of the grating lobes is unavoidable because the results from all transmission frequencies are used to synthesise the final result. In the

SCM-SA method, the SCM is applied to each echo that is received by each element, and the results obtained from the SCM then become the positive delay profile that is used for the subsequent SA technique. In this way, some of the effects of the grating lobes can be reduced. However, cancellation of the positive and negative signals is less likely to occur in the SCM-SA method, which results in the range resolution becoming insufficiently sharp and in the generation of some artefacts. For the SCM-weighted SA method, because the echo signal that is weighted by the SCM results is then applied to the SA, a sharp signal can be obtained. Even in the SCM-SA and SCM-weighted SA methods, when a high-frequency echo is used for the SA, grating lobes are still generated. In future work, appropriate integration of high-resolution images without these grating lobes may lead to better imaging results.

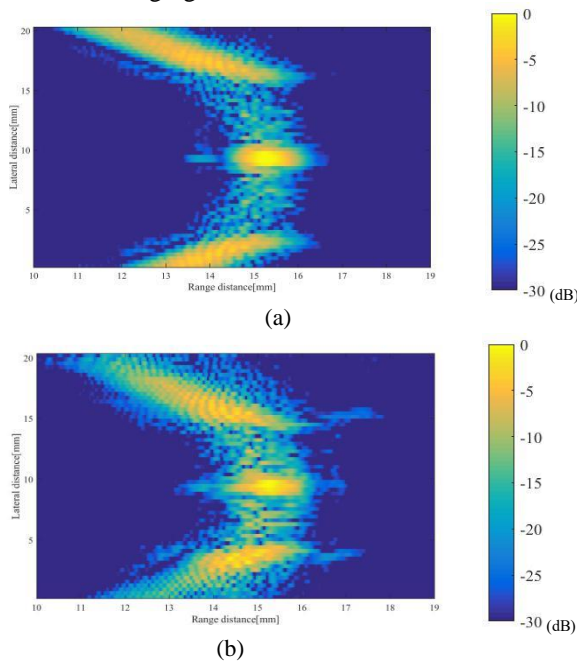


Fig. 7. Images showing SA method results: (a) SA at transmission frequency of 7.5 MHz; (b) SA at transmission frequency of 9.5 MHz.

Figure 8(e) shows the range profile results recorded at a depth of 15 mm. When compared with the SA results, the range resolution obviously improved when the SCM-SA and SCM-weighted SA methods were used. Observation of the reduction in the half-width of the main lobe confirms that the SCM-SA and SCM-weighted SA methods produced reductions of approximately 59% and 62%, respectively, but the SA-SCM caused the half-width to be reduced by approximately 64%. This difference in range resolution indicates that the SCM-SA and SCM-weighted SA methods are slightly inferior to the SA-SCM method. However, the most significant discrepancy among these methods occurs in the lateral direction, as shown in Fig. 8. The SA-SCM shows image discontinuities, whereas such discontinuities are unlikely to occur for both the SCM-SA and SCM-weighted SA methods. Because the target cannot be distinguished using the SA-SCM, better lateral resolution is

demonstrated by both the SCM-SA and SCM-weighted SA methods.

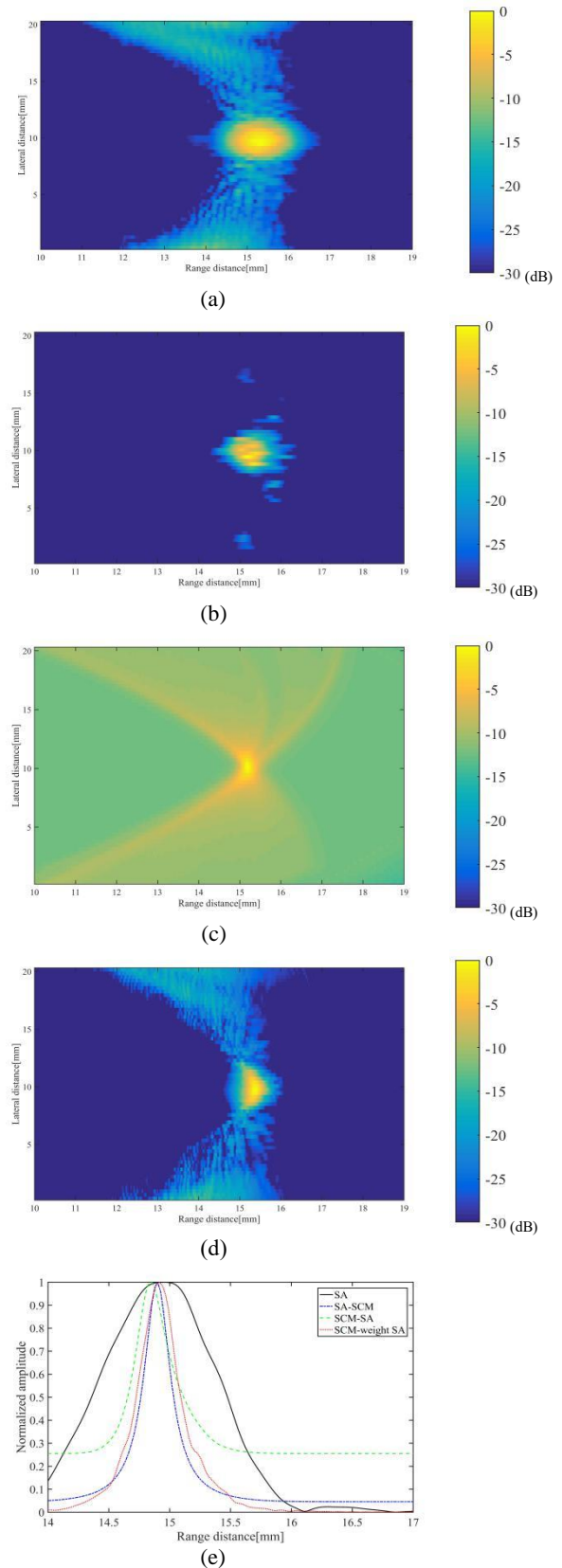


Fig. 8. Images of experimental results for: (a) SA method; (b) SA-SCM method; (c) SCM-SA method; (d) SCM-weighted SA method; and (e) comparison of the range resolutions of the various B-mode images.

The processing times required to form one B-mode image based on use of an Intel® core i7-4770 central processing unit (CPU) are listed in Table 1. Comparison of the two enhancement methods that are proposed in this study shows that the processing speed of the SCM-SA method is faster. The SA-SCM requires such great computational costs because it generates the results via line processing. It is possible that this time burden could be removed through use of the SCM-SA and SCM-weighted SA methods, because they generate their results via element processing.

TABLE 1. PROCESSING TIMES REQUIRED FOR ONE EXPERIMENTAL IMAGE

Method	SA	SA-SCM	SCM-SA	SCM-weighted SA
Time (sec.)	52	4649	349	357

#### IV. SIMULATIONS

##### A. Simulation Conditions

Given the limitations of the experimental system used for transmission of the FM chirps, the transmission waveform may become distorted. Therefore, it is necessary to confirm the effectiveness of the proposed methods through simulations using PZFlex (Weidlinger Associates Inc.), which is a time-domain finite element analysis simulator that can be used to analyse piezoelectric materials, ultrasound propagation, NDT and medical ultrasound problems [20].

##### B. Simulation Set-up

The simulation set-up used is the same as that shown in Fig. 4. Ideal FM chirp pulses were emitted towards a wide range region that was formed using a linear array transducer model with eight central vibration elements composing the sub-aperture, while reception was performed using 64 elements. Both the elements and the spacers have widths of 0.1575 mm, which means that the interval between elements is 0.315 mm. A target with a diameter of 1.5 mm, density of 7690 kg/m<sup>3</sup> and a speed of sound of 5900 m/s is located 15 mm away from the transducer in the area that is filled with water, which has a density of 1000 kg/m<sup>3</sup> and a speed of sound of 1500 m/s. We vary the centre frequency of the transmitted signal randomly 15 times from 4 MHz to 10 MHz. With the exception of the transmission waveform shown in Fig. 9, all conditions were as far as possible the same as those that were used in the prior experiments.

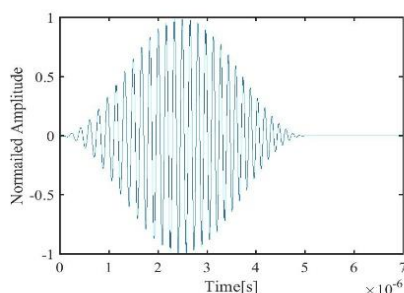


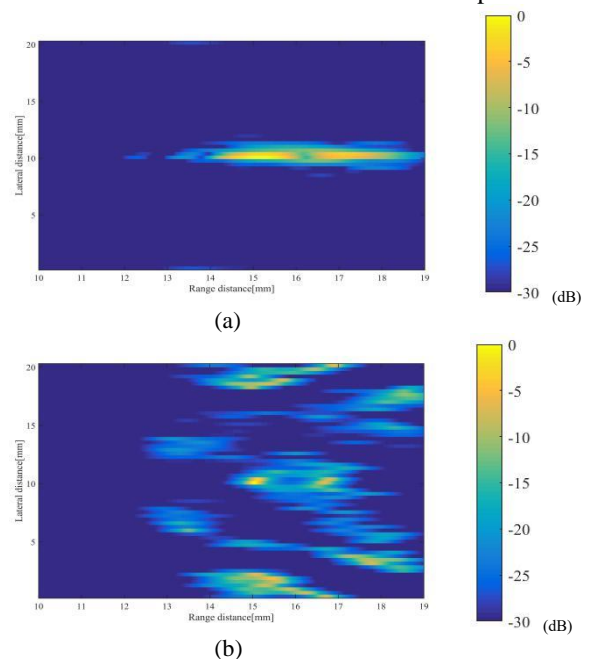
Fig. 9. Example of transmitted signal used for simulations.

##### C. Simulation Results

In the simulation results, in a manner similar to the earlier experimental results, the eigenvalues that correspond to the signal subspace that was calculated via SCM processing in the simulation are all sufficiently large at  $D=2$ , so we set  $D=2$  uniformly for all SCM processing.

Figure 10(a)–(d) show the B-mode images obtained from the SA, the SA-SCM, the SCM-SA and the SCM-weighted SA methods, respectively. The B-mode images of the SA, the SCM-SA and the SCM-weighted SA methods were all generated as averages of 15 images. Figure 10(e) shows a comparison result in the range direction, where the half-width of the front main lobe obtained when using the SCM-SA and SCM-weighted SA methods is reduced by approximately 71%, but the same half-width is reduced by approximately 82% when the SA-SCM is used. Additionally, the half-width of the back main lobe when using the SCM-SA and SCM-weighted SA methods is reduced by approximately 77% and 75%, respectively, while that for the SA-SCM is reduced by approximately 82%. Therefore, we can state that range resolution enhancement can be expected in the SA-SCM when compared with the SCM-SA and SCM-weighted SA methods.

In Fig. 10(e), the two wave profiles obtained from the front and back interfaces of the target are shown and illustrates that these profiles can be distinguished from each other more easily in the simulations than in the experiments. This is probably because the simulations only include the target material, i.e., the metal, while the experimental target has a vinyl layer around the metal rod. In future work, it will be necessary to perform these experiments after stripping the vinyl layer off the metal rod to determine whether the same results that were produced in the simulations can be obtained in practice.



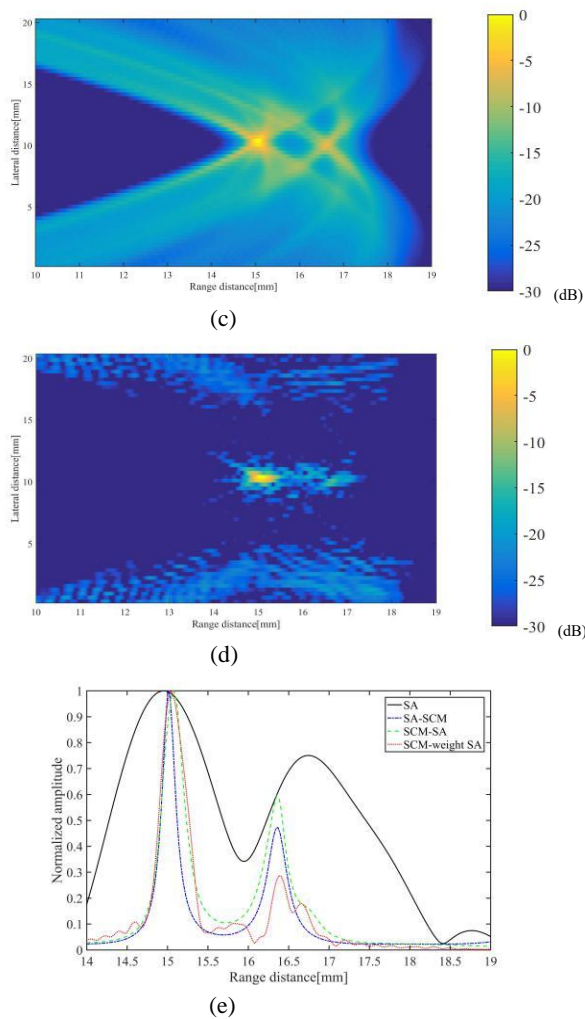


Fig. 10. Images of simulation results for: (a) SA method; (b) SA-SCM method; (c) SCM-SA method; (d) SCM-weighted SA method; and (e) comparison of the range resolution of the B-mode images.

In contrast, while the SA-SCM offers better range resolution, the discontinuities and the grating lobes that occur when using this method are still remarkable, and the method cannot detect the target clearly in the lateral direction. This restriction makes the SA-SCM less comparable to the SCM-SA and SCM-weighted SA methods, in which these problems have been resolved in terms of reducing some of the effects of the grating lobes and the artefacts in the final image.

In the simulations, as expected, the time required to generate one image based on the SCM-SA and SCM-weighted SA methods was shorter than that required for image generation based on the SA-SCM. Clearly, use of the SCM-SA and SCM-weighted SA methods not only improves the resolution performance but also accelerates the processing speed dramatically.

### V. CONCLUSIONS

In this study, we have proposed new methods for ultrasound imaging based on the SCM-SA and SCM-weighted SA methods. The proposed methods present three major advantages: i) super-resolution in the range direction; ii) flexibility in terms of computational cost;

and iii) proper suppression of both the lateral discontinuities and the effects of the grating lobes. We illustrated the performance of our methods using both experimental and simulated data when using a strong reflector. In fact, the super range resolution that was achieved using both the SCM-SA and SCM-weighted SA methods was not as strong as that which had been achieved using the previous SA-SCM method. However, the most interesting result was that the SCM-SA and SCM-weighted SA methods both provided better lateral resolution and faster processing speeds when compared with the SA-SCM method. In addition, the SCM-weighted SA method eliminated the artefacts that occurred when using the SCM-SA method as far as possible. Therefore, the SCM-weighted SA method may have greater potential for computationally-efficient super-resolution ultrasound imaging.

The simulation results that were obtained during this study represent only a preliminary confirmation of the effectiveness of the proposed methods. The performance aspects that were affected by the sizes and the numbers of the elements [21] will require further investigation via simulations. For simplicity, we used the well-known DAS beamforming method for SA imaging here. In future studies, we will examine the effects of the proposed methods on the performance of minimum variance (MV) beamforming [22] and other adaptive beamforming techniques [23] [24] for SA imaging. Furthermore, these results confirm that the proposed methods only preserve the super-resolution in the range direction. In the next stage, we intend to explore application of the filtered-delay multiply and sum (FDMAS) method [25] to the SCM processing, which will allow further improvement in the lateral resolution.

### REFERENCES

- [1] D. Amy, E. Durante and T. Tot, "The lobar approach to breast ultrasound imaging and surgery." *Journal of Medical Ultrasonics*, 2015, 42(3), 331-339.
- [2] J. Ylitalo, "A fast ultrasonic synthetic aperture imaging method: application to NDT." *Ultrasonics*, 1996, 34(2-5), 331-333.
- [3] S.I. Nikolov and J.A. Jensen, "3D synthetic aperture imaging using a virtual source element in the elevation plane." *IEEE. Int. Ultrasonics Symp.*, 2000, (2), 1743-1747.
- [4] D.T. Yeh, O. Oralkan, I.O. Wygant, M. O'Donnell and B.T. Khuri-Yakub, "3-D ultrasound imaging using a forward-looking CMUT ring array for intravascular/intracardiac applications." *IEEE Trans. Ultrason. Ferroelectr. Freq. Contr.*, 53(6), 1202-1211 (2006).
- [5] K. Nagai, "A new synthetic-aperture focusing method for ultrasonic B-scan imaging by Fourier transform." *IEEE Transactions on Sonics and Ultrasonics*, 1985, 32(4), 531-536.
- [6] J.A. Jensen, S.I. Nikolov, K.L. Gammelmark and M.H. Pedersen, "Synthetic aperture ultrasound imaging." *Ultrasonics*, 2006, (44), e5-e15.
- [7] Y. Honjo, H. Hasegawa and H. Kanai, "Two-dimensional tracking of heart wall for detailed analysis of heart function at high temporal and spatial resolutions." *Jpn. J. Appl. Phys.*, 2010, 49(7S), 07HF14.

- [8] G. Matrone, et al. "Spatial coherence based beamforming in multi-line transmit echocardiography." IEEE. Int. Ultrasonics Symp., 2018, in press.
- [9] T.X. Misaridis, M.H. Pedersen and J.A. Jensen, "Clinical use and evaluation of coded excitation in B-mode images." IEEE. Int. Ultrasonics Symp., 2000, (2), 1689-1693.
- [10] M. O'Donnell, "Coded excitation system for improving the penetration of real-time phased-array imaging systems." IEEE Trans. Ultrason. Ferroelectr. Freq. Contr., 1992, 39(3), 341-351.
- [11] M. Fujiwawara, K. Okubo and N. Tagawa, "A novel technique for high resolution ultrasound imaging super resolution FM-Chirp correlation Method (SCM)." IEEE Int. Ultrasonics Symp., 2009, pp.2390-2393.
- [12] R.O. Schmidt, "Multiple emitter location and signal parameter estimation." IEEE Trans. Antennas and Propagation, 1986, (34), 276-280.
- [13] P. Stoica and A. Nehorai, "MUSIC, maximum likelihood, and Cramer-Rao bound." IEEE Trans. Acoust., Speech, Signal Processing, 1989, (37), 720-741.
- [14] T. Wada, Y. Ho, N. Tagawa and K. Okubo, "Extension of FM-Chirp super resolution imaging for ultrasound synthetic aperture system." IEEE. Int. Ultrasonics Symp., 4 pages, 2015.
- [15] T. Wada, Y. Ho, K.Okubo, N. Tagawa, and Y. Hirose, "High frame rate super resolution imaging based on ultrasound synthetic aperture scheme." Physics Procedia, 2015, (70), 1216-1220.
- [16] B.D. Van Veen and K.M. Buckley, "Beamforming: a versatile approach to spatial filtering." IEEE ASSP Mag., 1988, 5(2), 4-24.
- [17] M.H. Bae and M.K. Jeong, "A study of synthetic-aperture imaging with virtual source elements in B-mode ultrasound imaging systems." IEEE Trans. Ultrason. Ferroelectr. Freq. Contr., 2000, (47), 1510-1519.
- [18] H. Bozdogan, "Model selection and Akaike's information criterion (AIC): The general theory and its analytical extensions." Psychometrika, 1987, (52), 345-370.
- [19] A. Barron, J. Rissanen and B. Yu, "The minimum description length principle in coding and modeling." IEEE Trans. Inform. Theory, 1998, 44(6), 2743-2760.
- [20] G.L. Wojcik, D.K. Vaughan, N. Abboud and J. Mould, "Electromechanical modelling using explicit time-domain finite elements." Proc. IEEE Ultrasonics Symp., 1993, (2), 1107-1112.
- [21] H. Hasegawa and C. L. de Korte, "Impact of element pitch on synthetic aperture ultrasound imaging." *Journal of Medical Ultrasonics*, 2016, 43, 317-352.
- [22] I.K. Holfort, F. Gran and J.A. Jensen, "Minimum variance beamforming for high frame-rate ultrasound imaging." IEEE Int. Ultrasonics Symp., 2007, pp.1541-1544.
- [23] H. Taki, K. Taki and M. Yamakawa et al. "High-range-resolution imaging using frequency domain interferometry with stabilization techniques for real-time vascular ultrasound." *Jpn. J. Appl. Phys.*, 2015, 54, 07HF05.
- [24] S. Okumura, H. Taki and T. Sato, "Computational complexity reduction techniques for real-time and high-resolution medical ultrasound imaging using the beam-space Capon method." *Jpn. J. Appl. Phys.*, 2016, 55, 07KF07.
- [25] G. Matrone and A. Ramalli, "Spatial coherence of backscattered signals in multi-line transmit ultrasound imaging and its effect on short-lag filtered-delay multiply and sum beamforming." *Appl. Sci.*, 2018, 8(4), 486.